Laguerre−Gaussian-Domain Rotational Image Restoration beyond the Camera Response

Luyi Wang,|| Jiantao Ma,|| Junjie Guo, Dan Wei, Min Xiao, and Yong Zhang*

Read Online

ACCESS | Metrics & More | Article Recommendations | Supporting Information

ABSTRACT: It is a crucial task to capture clear pictures of fast-rotating objects for both scientific research and industrial manufacture. However, when the rotational speed exceeds the camera response, the recorded image generally suffers from motion blur. Particularly, the rotation-induced blur becomes severer along with the increasing radius. It still lacks an effective way to break the camera limitation and restore the image from rotational motion blur. Here, we propose and experimentally demonstrate a novel Laguerre−Gaussian (LG) domain rotational image restoration technique. In LG domain, the rotation introduces an additional phase into each azimuthal LG component of the image, resulting in motion blur. The blur factor of LG spectrum is related to the rotational speed, which can be precisely measured according to the rotational Doppler effect. After correcting the LG spectrum, we successfully recover the image of an object rotating at a constant or time-varying speed beyond the camera response. Our results provide a useful approach to record high-quality images of astronomical targets, biological molecules, and industrial centrifuges rotating at an ultrahigh speed.

KEYWORDS: *Laguerre−Gaussian domain, rotational Doppler effect, blur factor, image restoration, orbital angular momentum*

INTRODUCTION

Optical imaging is a useful technique to acquire object information in a noncontact and nondestructive way, which has been widely applied in microscopy,[1] biomedicine,[2,3] multiband imaging,[4,5] and sensing.[6] For example, a high-speed imaging system is developed for real-time monitoring of fast-rotating objects such as biological molecules, industrial centrifuges and turbines, and astronomical objects. During the exposure time of the camera, the relative motion between the camera and the rotating target results in a certain blur[7,8] and degrades the image quality. In principle, a short exposure time helps suppress the motion blur, which, however, normally requires to increase the ISO of the camera, leading to extra electronic noise and poor signal-to-noise ratio of the recorded images. In addition, due to the limited shutter speed, there exists a minimal exposure time for a given camera, which decides the upper speed limit to record a rotating object clearly. By developing advanced algorithms based on Fourier domain imaging processing, it is possible to significantly suppress some types of motion blurs. When one deals with rotational motion blurs, the situation becomes quite inconvenient. The rotation-induced blur is space-variant,[9,10] i.e., the blur degree increases along with the radius, which hinders the traditional imaging recovery approaches based on the direct deconvolution in Fourier domain.[7,8,11−14] It still lacks an effective way to break the performance limitation of
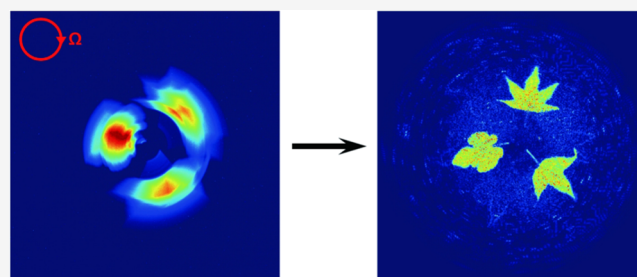
cameras and improve the image quality of high-speed rotating objects.

Laguerre−Gaussian (LG) modes are the Eigen solutions of the paraxial wave equation, which are capable of composing a complete and orthogonal basis to form arbitrary optical fields.[15−20] LG mode features a circular symmetry, which is characterized by an azimuthal index *l* (i.e., orbital angular momentum (OAM))[21,22] and a radial index *p*. By utilizing the *l* index, researchers have developed digital spiral imaging (DSI) techniques[23] to analyze the object's azimuthal information.[24−31] One can also input an OAM-carrying light to measure the rotational speed[32,33] based on the rotational Doppler effect.[34−37] Recently, the measurement of full LG spectrum has been demonstrated to reconstruct the image of a rotating object within the camera response speed.[38]

In this article, we propose and experimentally demonstrate a novel LG-domain image processing method to restore the rotation-blurred image beyond the camera response. The process of capturing an optical image of a rotating object is equivalent to an integration during the exposure time. Figure 1
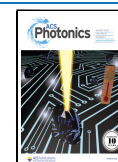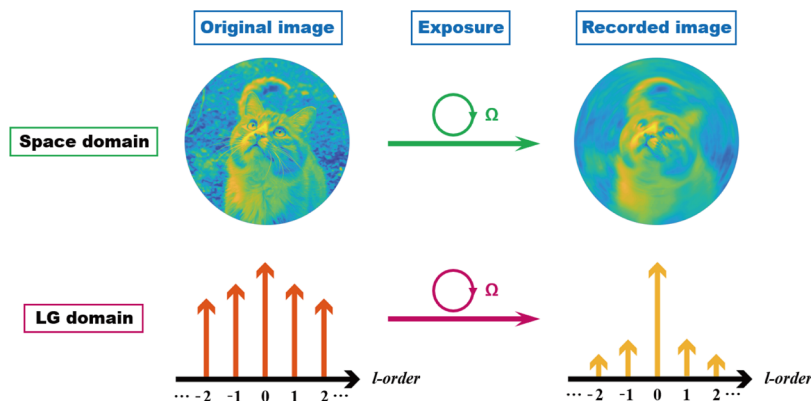
Figure 1. Scheme to capture optical image of a rotating object. The camera-recorded image is the time integration of the rotating optical field during the exposure time. As a result, one obtains a blurry image in space domain, in which the blur degree rapidly increases along the radial direction. In LG domain, the spectral weight is concentrated to low-order l components.
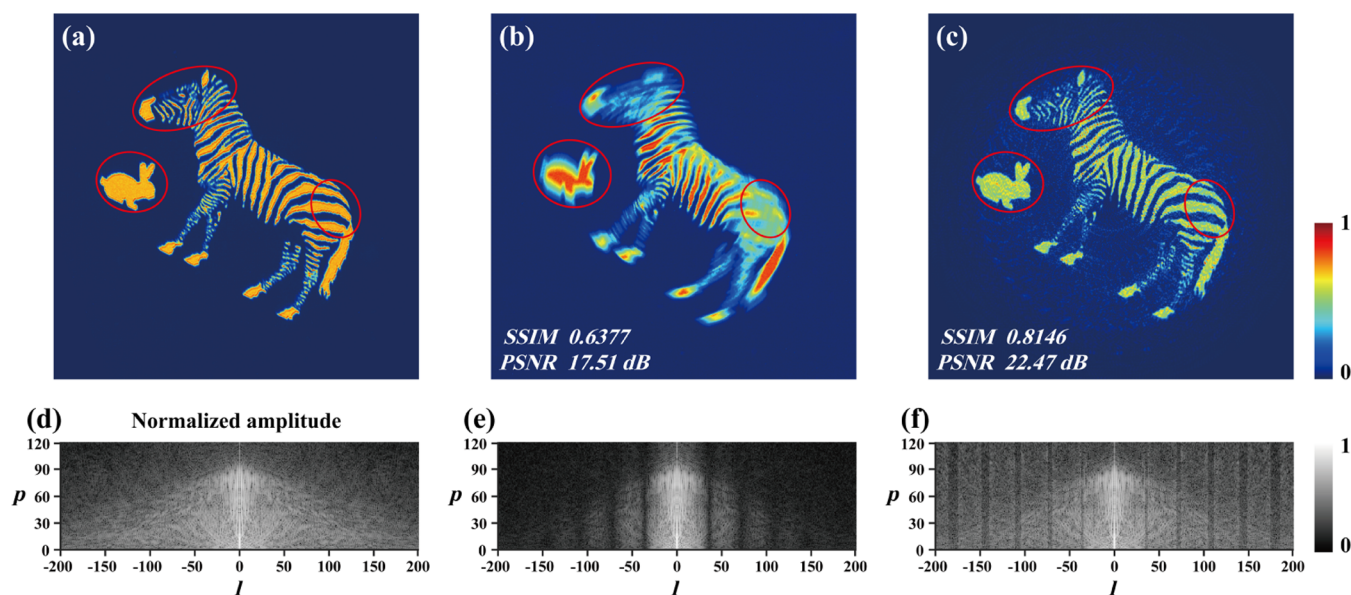

Figure 2. Experiment results of imaging an object rotating at a rotational frequency of 5 Hz. (a) Image of the stationary object. (b) Obtained image as it is rotating. The object rotates 10° during the exposure time of 1/180 s. (c) Reconstructed image by LG-domain recovery (see eq 5). The image is well restored, particularly in the severely blurred outer area (marked by red circles). Panels (d)−(f) show the amplitudes of the LG spectra of panels (a)−(c), respectively.

shows the typical process of recording an image of a rotating object. In real space, one obtains an obscure image in which the outer area is completely indistinguishable. In LG domain, the spectral distribution concentrates to the low-order l components. According to LG transform theory,[38] the function of rotation is to introduce an extra phase (relating to the rotational speed) into each l component while keeping the amplitude spectrum in LG domain. By real-time monitoring of the rotational speed, one can precisely calculate such additional phase and recover the image in LG domain. Such unique characteristics benefits from the circular symmetry of LG mode, providing a potential solution to suppress the rotational motion blur. In the experiment, we successfully demonstrate the image restoration under constant and time-varying rotational speeds, which paves the way to observe ultra-high-speed rotating objects beyond the camera response.

■ THEORY

When inputting a laser beam onto a stationary object, the obtained optical field (U_0) can be decomposed by using LG basis (see the Methods section)

$$U_0(r, \varphi) = \sum_l \sum_p A_{l,p} \mathrm{LG}_{l,p}(r)\exp(il\varphi) \tag{1}$$

where $A_{l,p}$ is the complex coefficient of LG spectrum. Consider that the object rotates at an angular velocity of Ω. According to the rotational Doppler effect,[32] each l component carries a frequency shift of $l\Omega$. So, the rotating optical field can be written as

$$U_t(r, \varphi, t) = \sum_l \sum_p A_{l,p} \mathrm{LG}_{l,p}(r)\exp(il\varphi)\exp(il\Omega t) \tag{2}$$

Clearly, the rotation produces a light field having the same LG amplitude spectrum except for an extra phase for each l component. Such a unique feature of LG basis results from its circularly symmetric profile.
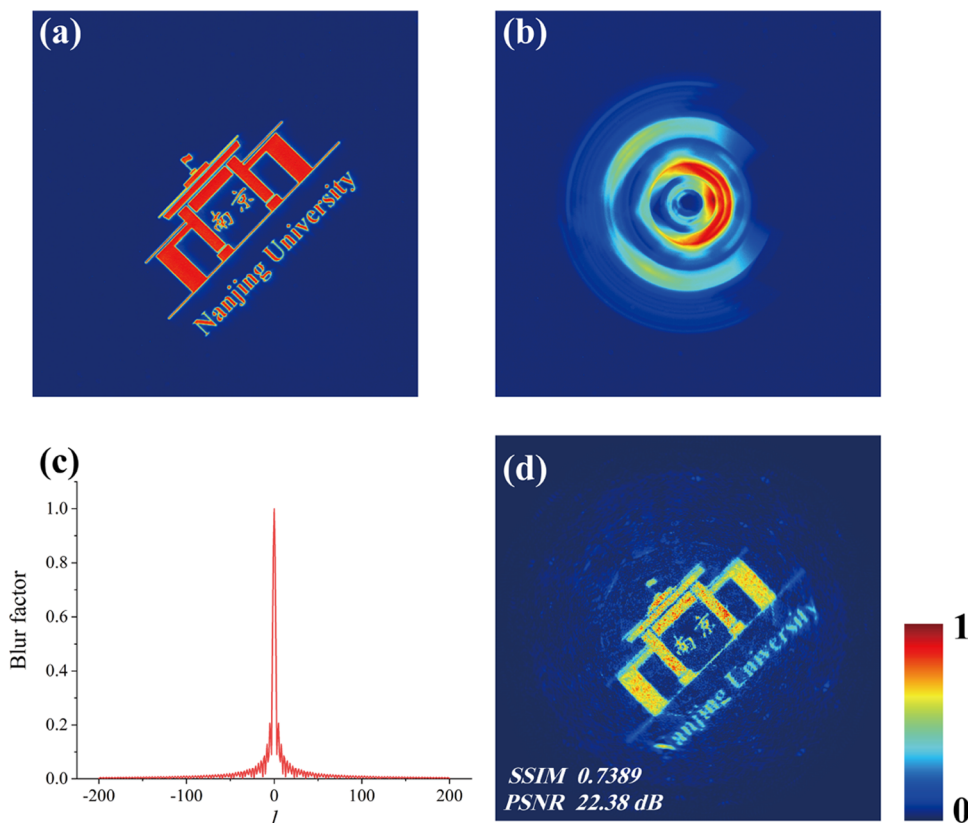
Figure 3. Experiment results of imaging a fast-rotating object at a rotational frequency of 55 Hz. (a) Original image. (b) Obtained image as the object is rotating. The object rotates 110° during the exposure time of 1/180 s. The image details are completely indistinguishable. (c) Calculated blur factor for each l component. (d) Clear image restored by LG-domain recovery based on eq 6. See Supporting Information Figure S3 for the comparison of OAM spectra.

An optical image is captured by a camera within an exposure time of T. The recorded image U_b can be calculated from the time integration of eq 2

$$U_b(r, \varphi) = \int_0^T U_t(r, \varphi, t) \, dt$$

$$= \sum_l \sum_p \int_0^T \exp(il\Omega t) \, dt \cdot A_{l,p} \mathrm{LG}_{l,p}(r) \exp(il\varphi) \tag{3}$$

Comparing eqs 1 and 3, one can deduce that the rotational-motion-induced blur results from the integration term (i.e., the blur factor) in eq 3. The object rotates an angle of $\theta = \Omega T$ during the exposure time T. The blur factor is calculated to be

$$F_{\mathrm{blurring}} = \int_0^T \exp(il\Omega t) \, dt = \int_{-\theta/2}^{\theta/2} \exp(il\alpha) \, d\alpha$$

$$= \theta \cdot \sin c(l\theta/2) \tag{4}$$

For convenience, we assume that the object rotates from $-\theta/2$ to $\theta/2$ within T. After correcting the measured LG spectrum by removing the blur factor, one can restore a clear image through LG-domain inverse filtering.

■ RESULTS AND DISCUSSION

The experimental setup is shown in Supporting Information Figure S1 (see the Methods section). There are two optical paths. In one path, we use an 808 nm laser as the light source to capture the image of a high-speed rotating object by a camera. In the other path, we input a 1064 nm laser to measure

the angular velocity of the rotating object based on the rotational Doppler effect (see the Methods section). The rotating object is simulated by using a digital micromirror device (DMD) (see the Methods section). The exposure time of the camera is set to $T = 1/180$ s.

Consider a slowly rotating object. The original object is shown in Figure 2a, and the recorded image is shown in Figure 2b. We measure the rotational frequency as 5 Hz and calculate the blur factor F_{blurring} (see Supporting Information Figure S2 and the Methods section). Then, we decompose the recorded image of Figure 2b in LG-mode basis. After considering the computing efficiency, the mode number should be large enough to guarantee the coverage of the image area and a good image quality. Here, we choose l ranging from -200 to 200 and p ranging from 0 to 120. The beam waist is set to $400 \ \mu$m. Notably, the sinc function in eq 4 (see the Methods section) could produce zero values in specific OAM orders, which may lead to unexpected background noises. To solve this issue, we set a threshold blur factor F_{th} and correct the coefficient of LG spectrum to

$$A_{l,p}^c = \begin{cases} A_{l,p}^r / F_{\mathrm{blurring}} & \text{if } F_{\mathrm{blurring}} \geq F_{\mathrm{th}} \\ A_{l,p}^r & \text{if } F_{\mathrm{blurring}} < F_{\mathrm{th}} \end{cases} \tag{5}$$

Here, $A_{l,p}^r$ is the measured LG spectrum of Figure 2b, and F_{th} is optimized as 0.03 in our experiment. After revising the LG spectrum based on eqs 4 and 5, we perform the inverse filtering operation and recover the image, as shown in Figure 2c. Here, we use structural similarity (SSIM)[39] and peak signal-to-noise
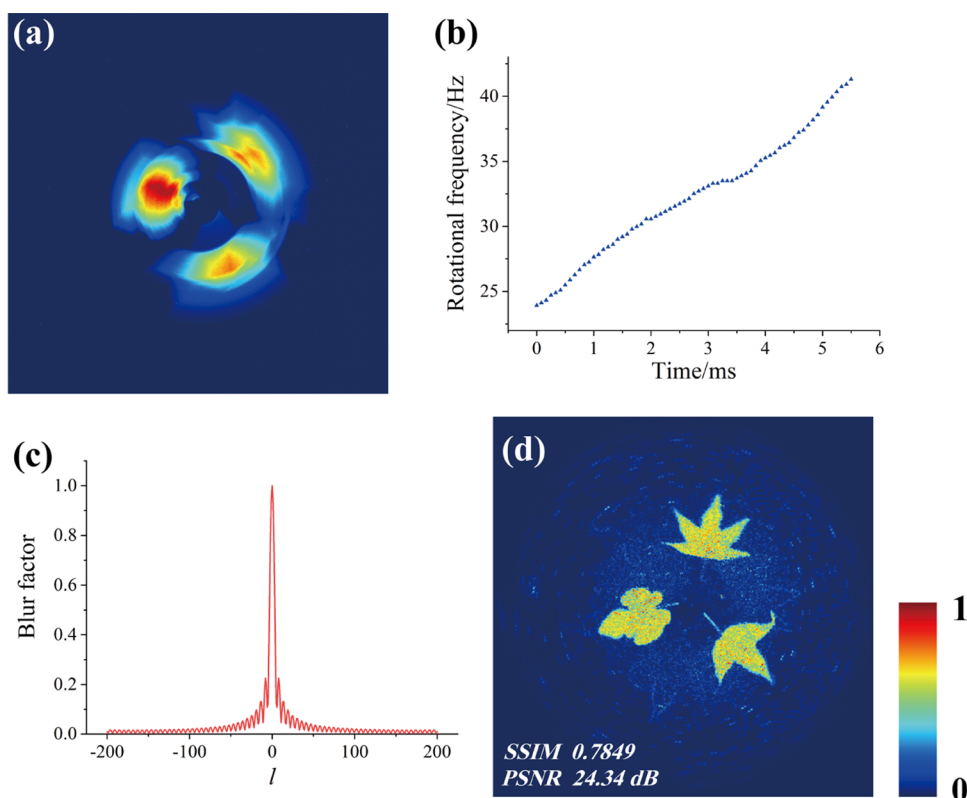
Figure 4. Experiment results of imaging a rotating object with a time-varying rotational frequency. (a) Recorded image of the rotating object. (b) Measured rotational frequency during the camera exposure time of 5.6 ms. (c) Calculated blur factor for each l component. (d) Restored images by LG-domain recovery. See Supporting Information Figure S4 for the comparison of OAM spectra.

ratio (PSNR)[40] to evaluate the image quality. The recovered image has an improved SSIM of 0.8146 and PSNR of 22.47 dB. Figure 2d−f shows the amplitude of the LG spectrum of the original object, the recorded image, and the recovered image, respectively. One can see that most of the LG spectrum has been corrected except for those orders with nearly zero value. By comparing Figure 2b,c, one can observe a clear improvement, especially in the marked areas.

Next, we investigate the performance of our approach at a higher rotational frequency of 55 Hz (Figure 3). The original image is shown in Figure 3a. The recorded image under $\theta = \Omega T = 110°$ is shown in Figure 3b, in which it is impossible to identify any useful information. The calculated blur factor $F_{blurring}$ is close to zero in most of high-order modes (Figure 3c). In this case, the criteria in eq 5 to correct the LG spectrum cannot work as effectively as in Figure 2. Here, we apply the Wiener filtering[7,41] in LG domain to correct the LG spectrum

$$A_{l,p}^{c} = \frac{F_{blurring}^{*}}{|F_{blurring}|^{2} + \gamma} \cdot A_{l,p} \tag{6}$$

This equation is derived according to the theory of Wiener filtering. The parameter γ works as the reciprocal of signal-to-ratio in traditional Wiener filtering,[41] which is critical to suppress the noise. In our experiment, γ is optimized to 0.00025. Figure 3d illustrates the restoration of the blurry image in Figure 3b. From Figure 3d, one can clearly recognize the details, including the Chinese and English characters. It should be noted that eq 6 is a general correction function in our method. In the case of analyzing slowly rotating objects, eq

5 is more efficient because it is not required to correct the LG components with their blur factors below F_{th}.

Particularly, our method is capable of retrieving a clear imaging for a spinning object with a time-varying rotational velocity. The theoretical deduction is similar to the above equations except that the term ΩT is replaced by an integration of $\int_{0}^{T} \Omega(\tau) \, d\tau$ (see the Methods section). In the experiment, we record the image by using the 808 nm light path. Meanwhile, we monitor the intensity of the 1064 nm laser path in real time. Then, we obtain $\Omega(\tau)$ through short-time Fourier transform. As shown in Figure 4b, the rotational frequency gradually increases from 24 to 41 Hz during the exposure time. The calculated blur factor is shown in Figure 4c. By applying Wiener filtering in LG domain, we successfully recover the image of three leaves (Figure 4d).

■ CONCLUSIONS

In this article, we propose and experimentally demonstrate a novel LG-domain image restoration technique. By utilizing the rotation-invariant profile and rotational Doppler frequency shift of LG mode, we have successfully deduced the rotation-induced blur factor and reconstructed the image accordingly. In Supporting Information Figure S5, we further analyze the performance of our scheme by comparing the reconstructed image with those slightly blurred images (captured as the object rotates an angle of $\theta = 1−3°$ during the exposure time). The results show that our method can effectively recover the severely blurred image ($\theta = 100−120°$) to a level that is acceptable to human eyes. Currently, our approach is mainly limited by the camera resolution and the measurement

precision of the rotational speed. Generally, the signal-to-noise ratio of the recorded signal decreases when increasing the rotational speed, which results in a certain decrease in image quality. The camera resolution decides the capacity of spatial information as well as the accuracy of analyzing the LG spectrum of the recorded image. The measurement of rotational speed is directly related to precise calculation of the blur factor. In our method, it is measured by a single-point detector, which can have a response much faster than a camera. In technique, one can combine a camera of high spatial resolution (for example, 6×10^7 pixels is available in commercial products) with a high-speed single-point detector (for example, 100 GHz is available in commercial products) to break the limitation of the camera itself and obtain a high-quality image of a rotating object. Our method provides a promising and effective way for real-time monitoring of rotational targets in scientific research and industrial equipment, especially those ultra-fast-rotating ones beyond the performance of traditional optical imaging systems.

■ METHODS

Experimental Setup. Our experiment setup is depicted in Supporting Information Figure S1. There are two optical routes for optical imaging and the measurement of angular velocity, respectively. In this work, we use the theory of rotational Doppler effect to measure the rotational speed, which requires a highly coherent input light to achieve a clear interference pattern. In optical imaging, a partially coherent light helps remove the speckles as well as improve the image quality. Therefore, we use a partially coherent laser working at 808 nm for optical imaging and a coherent laser working at 1064 nm to measure the rotating velocity. These input beams are combined together by a dichromatic mirror. A computer-controlled DMD (Texas Instruments DLP7000) is used to simulate a spinning object. After being modulated by DMD, the beams go through a 4f-imaging system and then are separated at another dichromatic mirror. The 808 nm light is directly recorded by a CCD camera that is placed on the imaging plane. The 1064 nm laser beam is projected onto a spatial light modulator (SLM). The SLM is encoded by a computer-generated hologram, i.e., the superposition of two OAM beams ($l_1 = 0$, $l_2 = 30$). After the SLM, a lens and a pinhole are used to select the fundamental mode of the modulated beams. The output signals are collected by a photodiode and analyzed on an oscilloscope.

Decomposing a Rotating Image in LG Domain. When inputting a laser beam onto a stationary object, the obtained optical field (U_0) can be decomposed by using LG-mode basis

$$U_0(r, \varphi) = \sum_l \sum_p A_{l,p} \mathrm{LG}_{l,p}(r)\exp(il\varphi)$$
$$= \sum_l B_l(r)\exp(il\varphi) \qquad (7)$$

where $\mathrm{LG}_{l,p}(r) = \sqrt{\frac{2p!}{\pi(p+|l|)!}} \frac{1}{\omega_0} \left(\sqrt{2}\frac{r}{\omega_0}\right)^{|l|} L_p^{|l|}\left(2\frac{r^2}{\omega_0^2}\right)\exp\left(-\frac{r^2}{\omega_0^2}\right)$, with l and p being the azimuthal and radial indices, respectively. ω_0 is the beam waist, $L_p^{|l|}$ is the Laguerre polynomial, and $A_{l,p}$ is the complex LG spectrum coefficient of $U_0(r, \varphi)$ with $\sum_l \sum_p |A_{l,p}|^2 = 1$. We define the azimuthal components as

$$B_l(r) = \sum_p A_{l,p} \mathrm{LG}_{l,p}(r) \qquad (8)$$

which represents the overall contributions from the LG modes with the same l but different p. If the object rotates at an angular velocity of Ω, according to the rotational Doppler effect,[32] each LG component has a frequency shift $l\Omega$ (independent of the p component). So, the rotating field at time t can be written as

$$U_t(r, \varphi, t) = \sum_l B_l(r)\exp(il\varphi)\exp(il\Omega t)$$
$$= \sum_l \sum_p A_{l,p} \mathrm{LG}_{l,p}(r)\exp(il\varphi)\exp(il\Omega t) \qquad (9)$$

If the angular velocity changes with time, i.e., $\Omega = \Omega(\tau)$, eq 9 should be rewritten to

$$U_t(r, \varphi, t) = \sum_l \sum_p A_{l,p} \mathrm{LG}_{l,p}(r)\exp(il\varphi)$$
$$\exp\left(il \int_0^t \Omega(\tau)\, \mathrm{d}\tau\right) \qquad (10)$$

In comparison to eq 1, the rotation produces a light field having the same amplitude spectrum of LG mode except for an extra phase for each l component.

Rotational Doppler Effect. The rotational Doppler effect[33,37] can be observed when using OAM-carrying modes to detect a rotational object. Here, we use the scheme of using the superposition of two OAM modes

$$E_i(r, \varphi) = M_{n_1}(r)\exp(in_1\varphi) + M_{n_2}(r)\exp(in_2\varphi) \qquad (11)$$

where n_1 and n_2 are the topological charges and $M(r)$ is the radial distribution of OAM mode. According to eq 2, the output field after being reflected by DMD (i.e., the rotating object) and SLM (i.e., the superposition of two OAM modes) can be expressed as

$$E_s(r, \varphi) = E_i(r, \varphi)U_t(r, \varphi, t)$$
$$= \sum_l \{M_{n_1}(r)B_l(r)\exp[i(n_1 + l)\varphi]\exp(il\Omega t)$$
$$+ M_{n_2}(r)B_l(r)\exp[i(n_2 + l)\varphi]\exp(il\Omega t)\} \qquad (12)$$

After spatial mode filtering, a single-point detector is used to detect the fundamental components of the output field. The intensity signal can be expressed as

$$I_s(t) = \iint r\, \mathrm{d}r\, \mathrm{d}\theta(|M_{n_1}(r)B_{-n_1}(r)|^2 + |M_{n_2}(r)B_{-n_2}(r)|^2)$$
$$+ 2\iint r\, \mathrm{d}r\, \mathrm{d}\theta|M_{n_1}(r)M_{n_2}^*(r)B_{-n_1}(r)B_{-n_2}^*(r)|$$
$$\cos[(n_1 - n_2)\Omega t + \phi(r)] \qquad (13)$$

where $\phi(r) = \mathrm{angle}[M_{n_1}(r)M_{n_2}^*(r)B_{-n_1}(r)B_{-n_2}^*(r)]$ is the relative phase between two OAM modes. Since the rotational Doppler effect is only related to the OAM component of the light field, eq 13 is simplified to

$$I_s(t) = |M_{n_1}B_{-n_1}|^2 + |M_{n_2}B_{-n_2}|^2 + 2|M_{n_1}M_{n_2}B_{-n_1}B_{-n_2}|$$
$$\cos[(n_1 - n_2)\Omega t + \phi] \qquad (14)$$

After Fourier transform, the frequency shift Δf of the output signal is positively correlated with $(n_1 - n_2)$. Then, the rotational speed of the object can be obtained by $\Omega = \Delta f/(n_1 - n_2)$. It should be noted that one can use the pixelated phase computer hologram[42] to generate the complex-amplitude field of eq 11 by using a phase-only SLM. In our experiment, we utilize the performance of SLM. Considering the modulation efficiency of SLM in our experiment, 90% of the reflected light is modulated to an OAM mode of $l = 30$, while the rest 10% is unmodulated Gaussian mode ($l = 0$). Although the interference pattern is not ideal, it is enough to extract the AC frequency component in eq 14.

Simulation of Rotational Objects with DMD. In our experiment, we use DMD to continuously play a series of preloaded patterns. For example, the pattern in Figure 2 rotates at a stable frequency of 5 Hz. We have prepared 1000 patterns to simulate a complete rotation cycle. The rotational angle of each pattern increases at a step of 0.36°. Each pattern is played on DMD with a duration of $t_1 = 0.2$ ms. When simulating a time-varying rotational object in Figure 4, we have prepared 360 patterns with different angles. Here, each pattern is played on DMD with a duration of $t_2 = 5/54$ ms. The rotational angle of the loaded pattern is decided by $\theta_i = 2\pi f_i t_2 + \theta_{i-1}$, where f_i is the instantaneous rotational frequency and θ_i and θ_{i-1} are the rotational angles of two sequential patterns.

ASSOCIATED CONTENT

SI Supporting Information

The Supporting Information is available free of charge at https://pubs.acs.org/doi/10.1021/acsphotonics.3c00192.

Experimental setup; measurement of the rotational frequency and blur factor; comparison of the OAM spectra; and evaluation of the performance of LG-domain filtering (PDF)

AUTHOR INFORMATION

Corresponding Author

Yong Zhang − *National Laboratory of Solid State Microstructures, College of Engineering and Applied Sciences, and Collaborative Innovation Center of Advanced Microstructures, Nanjing University, Nanjing 210093, China; School of Electronic Engineering & Intelligentization, Dongguan University of Technology, Dongguan 523808 Guangdong, China;* orcid.org/0000-0003-1158-2248; Email: zhangyong@nju.edu.cn

Authors

Luyi Wang − *National Laboratory of Solid State Microstructures, College of Engineering and Applied Sciences, and Collaborative Innovation Center of Advanced Microstructures, Nanjing University, Nanjing 210093, China*

Jiantao Ma − *National Laboratory of Solid State Microstructures, College of Engineering and Applied Sciences, and Collaborative Innovation Center of Advanced Microstructures, Nanjing University, Nanjing 210093, China*

Junjie Guo − *National Laboratory of Solid State Microstructures, College of Engineering and Applied Sciences, and Collaborative Innovation Center of Advanced Microstructures, Nanjing University, Nanjing 210093, China*

Dan Wei − *School of Electronic Engineering & Intelligentization, Dongguan University of Technology, Dongguan 523808 Guangdong, China*

Min Xiao − *National Laboratory of Solid State Microstructures, College of Engineering and Applied Sciences, and Collaborative Innovation Center of Advanced Microstructures, Nanjing University, Nanjing 210093, China; Department of Physics, University of Arkansas, Fayetteville, Arkansas 72701, United States*

Complete contact information is available at: https://pubs.acs.org/10.1021/acsphotonics.3c00192

Author Contributions

‖L.W. and J.M. contributed equally to this work.

■ REFERENCES

(1) Huisken, J.; Swoger, J.; Del Bene, F.; Wittbrodt, J.; Stelzer, E. H. K. Optical sectioning deep inside live embryos by selective plane illumination microscopy. *Science* **2004**, *305*, 1007−1009.

(2) Freudiger, C. W.; Min, W.; Saar, B. G.; Lu, S.; Holtom, G. R.; He, C.; Tsai, J. C.; Kang, J. X.; Xie, X. S. Label-Free Biomedical Imaging with High Sensitivity by Stimulated Raman Scattering Microscopy. *Science* **2008**, *322*, 1857−1861.

(3) Xu, M. H.; Wang, L. H. V. Photoacoustic imaging in biomedicine. *Rev. Sci. Instrum.* **2006**, *77*, No. 041101.

(4) Rieke, G. H.; Young, E. T.; Engelbracht, C. W.; Kelly, D. M.; Low, F. J.; Haller, E. E.; Beeman, J. W.; Gordon, K. D.; Stansberry, J. A.; Misselt, K. A.; et al. The Multiband Imaging Photometer for Spitzer (MIPS). *Astrophys. J. Suppl. Ser.* **2004**, *154*, 25−29.

(5) Jepsen, P. U.; Cooke, D. G.; Koch, M. Terahertz spectroscopy and imaging - Modern techniques and applications. *Laser Photonics Rev.* **2011**, *5*, 124−166.

(6) Poh, M.-Z.; McDuff, D. J.; Picard, R. W. Non-contact, automated cardiac pulse measurements using video imaging and blind source separation. *Opt. Express* **2010**, *18*, 10762−10774.

(7) Rafael, C. G.; Richard, E. W. *Digital Image Processing*; Addison-Wesley, 1997.

(8) Banham, M. R.; Katsaggelos, A. K. Digital image restoration. *IEEE Signal Process. Mag.* **1997**, *14*, 24−41.

(9) Sawchuk, A. A. Space-variant image motion degradation and restoration. *Proc. IEEE* **1972**, *60*, 854−861.

(10) Sawchuk, A. A. Space-variant system-analysis of image motion. *J. Opt. Soc. Am.* **1973**, *63*, 1052−1063.

(11) Sawchuk, A. A. Space-variant image restoration by coordinate transformations. *J. Opt. Soc. Am.* **1974**, *64*, 138−144.

(12) Hong, H. Y.; Zhang, T. X. Fast restoration approach for rotational motion blurred image based on deconvolution along the blurring paths. *Opt. Eng.* **2003**, *42*, 3471−3486.

(13) Shan, Q.; Xiong, W.; Jia, J. In *Rotational Motion Deblurring of a Rigid Object from a Single Image*, 2007 IEEE 11th International Conference on Computer Vision; IEEE, 2007; pp 738−745.

(14) Han, C.; Li, J.; Chen, X.; Zhu, Z.; et al. Real-time restoration of rotational blurred image using gradient-loading. *Chin. Opt. Lett.* **2008**, *6*, 334−337.

(15) Yao, A. M.; Padgett, M. J. Orbital angular momentum: origins, behavior and applications. *Adv. Opt. Photonics* **2011**, *3*, 161−204.

(16) Xiao, Y.; Tang, X.; Wan, C.; Qin, Y.; Peng, H.; Hu, C.; Qin, B. Laguerre-Gaussian mode expansion for arbitrary optical fields using a subspace projection method. *Opt. Lett.* **2019**, *44*, 1615−1618.

(17) Li, F.; Xu, T.; Zhang, W.; Qiu, X.; Lu, X.; Chen, L. Optical images rotation and reflection with engineered orbital angular momentum spectrum. *Appl. Phys. Lett.* **2018**, *113*, No. 161109.

(18) D'Errico, A.; D'Amelio, R.; Piccirillo, B.; Cardano, F.; Marrucci, L. Measuring the complex orbital angular momentum spectrum and spatial mode decomposition of structured light beams. *Optica* **2017**, *4*, 1350−1357.

(19) Tan, H.; Deng, J.; Zhao, R. Z.; Wu, X.; Li, G. X.; Huang, L. L.; Liu, J.; Cai, X. A Free-Space Orbital Angular Momentum Multiplexing Communication System Based on a Metasurface. *Laser Photonics Rev.* **2019**, *13*, No. 1800278.

(20) Ma, J.; Wei, D.; Wang, L.; Zhang, Y.; Xiao, M. High-quality reconstruction of an optical image by an efficient Laguerre-Gaussian mode decomposition method. *OSA Continuum* **2021**, *4*, 1396−1403.

(21) Forbes, A.; de Oliveira, M.; Dennis, M. R. Structured light. *Nat. Photonics* **2021**, *15*, 253−262.

(22) Wan, C.; Cao, Q.; Chen, J.; Chong, A.; Zhan, Q. Toroidal vortices of light. *Nat. Photonics* **2022**, *16*, 519−522.

(23) Torner, L.; Torres, J. P.; Carrasco, S. Digital spiral imaging. *Opt. Express* **2005**, *13*, 873−881.

(24) Molina-Terriza, G.; Rebane, L.; Torres, J. P.; Torner, L.; Carrasco, S. Probing canonical geometrical objects by digital spiral imaging. *J. Eur. Opt. Soc., Rapid Publ.* **2007**, *2*, No. 07014.

(25) Yao, E.; Franke-Arnold, S.; Courtial, J.; Barnett, S.; Padgett, M. Fourier relationship between angular position and optical orbital angular momentum. *Opt. Express* **2006**, *14*, 9071−9076.

(26) Jack, B.; Padgett, M. J.; Franke-Arnold, S. Angular diffraction. *New J. Phys.* **2008**, *10*, No. 103013.

(27) Uribe-Patarroyo, N.; Fraine, A.; Simon, D. S.; Minaeva, O.; Sergienko, A. V. Object Identification Using Correlated Orbital Angular Momentum States. *Phys. Rev. Lett.* **2013**, *110*, No. 043601.

(28) Yang, Z.; Magana-Loaiza, O. S.; Mirhosseini, M.; Zhou, Y.; Gao, B.; Gao, L.; Rafsanjani, S. M. H.; Long, G.-L.; Boyd, R. W. Digital spiral object identification using random light. *Light: Sci. Appl.* **2017**, *6*, No. e17013.

(29) Xie, G.; Song, H.; Zhao, Z.; Milione, G.; Ren, Y.; Liu, C.; Zhang, R.; Bao, C.; Li, L.; Wang, Z.; et al. Using a complex optical orbital-angularmomentum spectrum to measure object parameters. *Opt. Lett.* **2017**, *42*, 4482−4485.

(30) Zhang, W.; Gao, J.; Zhang, D.; He, Y.; Xu, T.; Fickler, R.; Chen, L. Free-Space Remote Sensing of Rotation at the Photon-Counting Level. *Phys. Rev. Appl.* **2018**, *10*, No. 044014.

(31) Wang, L.; Ma, J.; Xiao, M.; Zhang, Y. Application of optical orbital angular momentum to rotation measurements. *Results Opt.* **2021**, *5*, No. 100158.

(32) Lavery, M. P. J.; Speirits, F. C.; Barnett, S. M.; Padgett, M. J. Detection of a Spinning Object Using Light's Orbital Angular Momentum. *Science* **2013**, *341*, 537−540.

(33) Zhai, Y.; Fu, S.; Yin, C.; Zhou, H.; Gao, C. Detection of angular acceleration based on optical rotational Doppler effect. *Opt. Express* **2019**, *27*, 15518−15527.

(34) Courtial, J.; Robertson, D. A.; Dholakia, K.; Allen, L.; Padgett, M. J. Rotational frequency shift of a light beam. *Phys. Rev. Lett.* **1998**, *81*, 4828−4830.

(35) Courtial, J.; Dholakia, K.; Robertson, D. A.; Allen, L.; Padgett, M. J. Measurement of the rotational frequency shift imparted to a rotating light beam possessing orbital angular momentum. *Phys. Rev. Lett.* **1998**, *80*, 3217−3219.

(36) Fang, L.; Padgett, M. J.; Wang, J. Sharing a Common Origin Between the Rotational and Linear Doppler Effects. *Laser Photonics Rev.* **2017**, *11*, No. 1700183.

(37) Zhou, H.; Fu, D.; Dong, J.; Zhang, P.; Zhang, X. Theoretical analysis and experimental verification on optical rotational Doppler effect. *Opt. Express* **2016**, *24*, 10050−10056.

(38) Wei, D.; Ma, J.; Wang, T.; Xu, C.; Zhu, S.; Xiao, M.; Zhang, Y. Laguerre-Gaussian transform for rotating image processing. *Opt. Express* **2020**, *28*, 26898−26907.

(39) Wang, Z.; Bovik, A. C.; Sheikh, H. R.; Simoncelli, E. P. Image quality assessment: from error visibility to structural similarity. *IEEE Trans. Image Process.* **2004**, *13*, 600−612.

(40) Sheikh, H. R.; Sabir, M. F.; Bovik, A. C. A statistical evaluation of recent full reference image quality assessment algorithms. *IEEE Trans. Image Process.* **2006**, *15*, 3440−3451.

(41) Rafael, C. G.; Richard, E. W.; Steven, L. E. *Digital Image Processing Using Matlab*; Prentice Hall, 2003.

(42) Arrizón, V.; Ruiz, U.; Carrada, R.; González, L. A. Pixelated phase computer holograms for the accurate encoding of scalar complex fields. *J. Opt. Soc. Am. A* **2007**, *24*, 3500−3507.

🕮 Recommended by ACS